INTERNATIONAL JOURNAL FOR NUMERICAL METHODS IN FLUIDS
Int. J. Numer. Meth. Fluids 2009; **60**:1200–1221
Published online 3 December 2008 in Wiley InterScience (www.interscience.wiley.com). DOI: 10.1002/fld.1928

Numerical solutions of liquid metal flows by incompressible magneto-hydrodynamics with heat transfer

Kenan Şentürk[1], Massimo Tessarotto[2] and Necdet Aslan[1,*,†]

[1]*Physics Department, Yeditepe University, Kayışdağı, 81120 İstanbul, Turkey*
[2]*Applied Mathematics Department, University of Trieste, Via A Valerio No. 12B Trieste, Italy*

SUMMARY

A two-dimensional incompressible magneto-hydrodynamic code is presented in order to solve the steady state or transient magnetized or neutral convection problems with the effect of heat transfer. The code utilizes a numerical matrix distribution scheme that runs on structured or unstructured triangular meshes and employs a dual time-stepping technique with multi-stage Runge–Kutta algorithm. The code can be used to simulate the natural convection with internal heat generation and absorption and nonlinear time-dependent evolution of heated and magnetized liquid metals exposed to external fields. Copyright © 2008 John Wiley & Sons, Ltd.

Received 8 February 2008; Revised 13 August 2008; Accepted 21 August 2008

KEY WORDS: liquid metal flow; magneto-hydrodynamics; matrix distribution; numerical method; incompressible; Navier–Stokes

1. MAGNETO-HYDRODYNAMIC EQUATIONS

In this work, it is assumed that the flow is characterized by two-dimensional (2D) incompressible Navier–Stokes–Fourier plus Maxwell equations in the quasi-static approximation (i.e. Magneto-hydrodynamic (MHD) equations). The MHD system is coupled with the temperature effects through gravitational force by means of the Bousinessq approximation. In addition, the fluid is assumed to be electrically conducting and locally quasi-neutral at the same time. As a consequence, not only the fluid flow contributes to the electric and magnetic field distributions in the medium but

*Correspondence to: Necdet Aslan, Physics Department, Yeditepe University, Kayışdağı, 81120 İstanbul, Turkey.
†E-mail: naslan@yeditepe.edu.tr

Contract/grant sponsor: University of Trieste
Contract/grant sponsor: ICTP, Italy
Contract/grant sponsor: Tubitak, Turkey; contract/grant number: TBAG-U/166 (105T547)

flow features can also be adjusted by the application of external electric and magnetic fields. The starting point for the derivations of MHD equations is the NS equations given by:

$$\vec{\nabla}\cdot\vec{\mathbf{V}}=0 \tag{1}$$

$$\rho\left(\frac{\partial\vec{\mathbf{V}}}{\partial t}+\vec{\mathbf{V}}\cdot\vec{\nabla}\vec{\mathbf{V}}\right)+\vec{\nabla}P-\rho\vec{g}=\vec{\mathbf{F}}_L=\mu\nabla^2\vec{\mathbf{V}}+\vec{\mathbf{J}}\times\vec{\mathbf{B}} \tag{2}$$

$$\rho C_v\left(\frac{\partial T}{\partial t}+\vec{\mathbf{V}}\cdot\vec{\nabla}T\right)=Q=q+\eta\vec{\mathbf{J}}\cdot\vec{\mathbf{J}}+\kappa\nabla^2T \tag{3}$$

where ρ is the mass density, $\vec{\mathbf{V}}$ is the velocity, P is the pressure, T is the temperature, $\vec{g}=-g\hat{j}$ is the gravitational acceleration in the vertical direction, C_v is the specific heat, Q is the heat generation rate, μ, κ, and η are viscosity, thermal conductivity and resistivity, respectively. The right-hand side of Equation (2) includes viscosity terms and Lorentz force due to the current density ($\vec{\mathbf{J}}$), which provides the link between the fluid conservation laws and the following Maxwell's equations:

$$\frac{\partial\vec{\mathbf{B}}}{\partial t}-\vec{\nabla}\times(\vec{\mathbf{V}}\times\vec{\mathbf{B}})-\frac{\eta}{\mu_0}\nabla^2\vec{\mathbf{B}}=\vec{S}_B \tag{4}$$

$$\vec{\nabla}\cdot\vec{\mathbf{B}}=0 \tag{5}$$

$$\mu_0\vec{\mathbf{J}}=\vec{\nabla}\times\vec{\mathbf{B}},\quad \vec{\nabla}\cdot\vec{\mathbf{J}}=0 \tag{6}$$

where μ_0 is magnetic permeability, $\vec{\mathbf{B}}$ is the magnetic field, and $\vec{S}_B$ is the source driving magnetic field. In addition to these equations, it is known that the current density also satisfies Ohm's law given by

$$\eta\vec{\mathbf{J}}^{\mathrm{T}}=\vec{\mathbf{E}}^{\mathrm{T}}+\vec{\mathbf{V}}\times\vec{\mathbf{B}}^{\mathrm{T}} \tag{7}$$

where the superscript denoted the total fields. This definition of the current density includes the effects of the external electric and magnetic fields existing around the flow region. By taking into account the external fields, $\vec{\mathbf{F}}_L$, Q and $\vec{S}_B$, in the above equations they turn respectively, into

$$\vec{\mathbf{F}}=-\rho\vec{g}+\vec{\mathbf{J}}^{\mathrm{T}}\times\vec{\mathbf{B}}^{\mathrm{T}},\quad Q=\eta\vec{\mathbf{J}}^{\mathrm{T}}\cdot\vec{\mathbf{J}}^{\mathrm{T}}+q,\quad \vec{S}_B=-\vec{\nabla}\times(\vec{\mathbf{V}}\times\vec{\mathbf{B}}^{\mathrm{ext}}) \tag{8}$$

where $\vec{\mathbf{B}}^{\mathrm{ext}}$ is the external magnetic field, $\vec{\mathbf{J}}^{\mathrm{T}}$, $\vec{\mathbf{E}}^{\mathrm{T}}$, and $\vec{\mathbf{B}}^{\mathrm{T}}$ are the total current density, electric field and magnetic field, respectively:

$$\vec{\mathbf{J}}^{\mathrm{T}}=\vec{\mathbf{J}}+\vec{\mathbf{J}}^{\mathrm{ext}},\quad \vec{\mathbf{E}}^{\mathrm{T}}=\vec{\mathbf{E}}+\vec{\mathbf{E}}^{\mathrm{ext}}\approx\vec{\mathbf{E}}^{\mathrm{ext}},\quad \vec{\mathbf{B}}^{\mathrm{T}}=\vec{\mathbf{B}}+\vec{\mathbf{B}}^{\mathrm{ext}} \tag{9}$$

Note that due to the localized charge neutrality the internal electric field is assumed to be negligible in comparison with the external electric field, $\vec{\mathbf{E}}^{\mathrm{ext}}$.

For the low-speed flows where the gravitational forces are comparable to inertia and viscous forces, and the temperature effects should be included in density. To account for these effects, the following Boussinesq approximation (BA) was used:

$$\rho=\rho_0[1-\beta_T(T-T_0)] \tag{10}$$

DOI: 10.1002/fld

where β_T is the expansion coefficient due to temperature and ρ_o and T_0 are reference density and temperature, respectively. In this case, the last two terms on the left-hand side of Equation (2) become:

$$\vec{\nabla} P - \rho_0 \vec{g} = \vec{\nabla}(P - P_0) = \vec{g}[\beta_T (T - T_0)] \tag{11}$$

where $\partial P/\partial x = 0$ and $\partial P/\partial y = \rho_0 g$ was used since $P_0 = \rho_0 g y$. In order to write in dimensionless form of the MHD equations the following dimensionless reduced pressure and temperature are used:

$$P' = P - P_0, \quad \theta = \frac{T - T_c}{T_h - T_c} \tag{12}$$

where T_h and T_c, denote respectively, 'hot' and 'cold' wall temperatures. In the work presented here, artificial compressibility [1] and artificial magnetic flux function [2] are used in order to handle the divergence conditions on velocity and magnetic fields by pseudo iterations. The modified divergence equations describing this procedure are given by:

$$\frac{\partial P'}{\partial \tau} + \beta^2 \left(\frac{\partial u}{\partial x} + \frac{\partial v}{\partial y} \right) = 0 \tag{13}$$

$$\frac{\partial \psi}{\partial \tau} + \delta^2 \left(\frac{\partial B_x}{\partial x} + \frac{\partial B_y}{\partial y} \right) = 0 \tag{14}$$

where β^2 is the artificial compressibility parameter, δ^2 is the magnetic relaxation constant and ψ is called artificial magnetic relaxation function. In the numerical procedure, these equations are iterated between each real time step until overall convergence is established in pseudo time, τ, so that $\partial \mathbf{U}/\partial \tau \to 0$ where $\mathbf{U}$ is the state vector defined in the subsequent pages. In order to have a stronger relaxation, the remaining original equations are also modified by adding their pseudo time rates. In such a case, the velocity and magnetic fields will have been made divergenceless before updating the state variables at the new time level. In addition to these modifications, a $\vec{\nabla}\psi$ term is added to Faraday's equation as well. This term acts as an auxiliary magnetic pressure turning into a Lagrange multiplier, which is used along with pseudo iterations (a similar idea was used in [2, 3]).

By using all the assumptions described so far the dimensionless MHD equations in cartesian geometry can be written as:

$$\frac{\partial P'}{\partial \tau} + \beta^2 \left(\frac{\partial u}{\partial x} + \frac{\partial v}{\partial y} \right) = 0 \tag{15}$$

$$\frac{\partial u}{\partial \tau} + \frac{\partial u}{\partial t} + u\frac{\partial u}{\partial x} + v\frac{\partial u}{\partial y} + \frac{\partial P'}{\partial x} + \frac{N}{Re_m} B_y^{\mathrm{T}} \left(\frac{\partial B_y}{\partial x} - \frac{\partial B_x}{\partial y} \right) = \frac{1}{Re} \nabla^2 u \tag{16}$$

$$\frac{\partial v}{\partial \tau} + \frac{\partial v}{\partial t} + u\frac{\partial v}{\partial x} + v\frac{\partial v}{\partial y} + \frac{\partial P'}{\partial y} - \frac{N}{Re_m} B_x^{\mathrm{T}} \left(\frac{\partial B_y}{\partial x} - \frac{\partial B_x}{\partial y} \right) = \frac{1}{Re} \nabla^2 v + \frac{Ra\Theta}{PrRe^2} \tag{17}$$

$$\frac{\partial \theta}{\partial \tau} + \frac{\partial \theta}{\partial t} + u\frac{\partial \theta}{\partial x} + v\frac{\partial \theta}{\partial y} = \frac{1}{RePr} \nabla^2 \theta + NE[E^{\mathrm{ext}2} + (uB_y{}^{\mathrm{T}} - vB_x{}^{\mathrm{T}})^2] + \frac{Ra^{\mathrm{i}}}{RaRePr} \tag{18}$$

DOI: 10.1002/fld

$$\frac{\partial B_x}{\partial \tau}+\frac{\partial B_x^{\mathrm{T}}}{\partial t}+u\frac{\partial B_x^{\mathrm{T}}}{\partial x}+v\frac{\partial B_x^{\mathrm{T}}}{\partial y}-B_x^{\mathrm{T}}\frac{\partial u}{\partial x}-B_y^{\mathrm{T}}\frac{\partial u}{\partial y}+\frac{\partial \psi}{\partial x}=\frac{1}{Re_{\mathrm{m}}}\nabla^2 B_x^{\mathrm{T}} \tag{19}$$

$$\frac{\partial B_y}{\partial \tau}+\frac{\partial B_y^{\mathrm{T}}}{\partial t}+u\frac{\partial B_y^{\mathrm{T}}}{\partial x}+v\frac{\partial B_y^{\mathrm{T}}}{\partial y}-B_x^{\mathrm{T}}\frac{\partial v}{\partial x}-B_y^{\mathrm{T}}\frac{\partial v}{\partial y}+\frac{\partial \psi}{\partial y}=\frac{1}{Re_{\mathrm{m}}}\nabla^2 B_y^{\mathrm{T}} \tag{20}$$

$$\frac{\partial \psi}{\partial \tau}+\delta^2\left(\frac{\partial B_x}{\partial x}+\frac{\partial B_y}{\partial y}\right)=0 \tag{21}$$

where Re is Reynolds number, Ra is Rayleigh number, Pr is the Prandtl number, N is the magnetic interaction parameter, Re_{m} is magnetic Reynolds number, Ra^{i} is the internal Rayleigh number, and E is Eckert number which are all defined as:

$$Pr=\frac{\nu}{k},\quad Ra=\frac{g\beta_T L^3\Delta T}{\kappa\nu},\quad Ra^{\mathrm{i}}=\frac{g\beta_T L^5 q}{\nu k\kappa} \tag{22a}$$

$$N=\frac{B_0^2 L_0}{\nu\rho_0 V_0},\quad E=\frac{V_0^2}{C_p\Delta T},\quad Re_{\mathrm{m}}=\frac{\mu_0 V_0 L_0}{\nu} \tag{23a}$$

where $\nu=\mu/\rho_0$ is the kinematic viscosity, $\kappa=k/\rho_0 C_p$ is the thermal diffusivity, and C_p is the specific heat at constant pressure.

The matrix distribution (MD) scheme presented here allows the implementation of different boundary conditions for the nodes along boundaries. If the nodes are untouched, the boundary simply becomes an outgoing boundary on which the behavior of nodal values is totally governed by interior values. This condition simply handles zero normal derivatives. No slip boundary condition is implemented by simply setting $u=v=0$ at the boundary nodes. Reflection boundary conditions can be devised by setting normal velocities to zero and leaving the other component untouched. For the non-conducting walls, the normal current density vanishes (i.e. $\vec{\mathbf{J}}\cdot\mathbf{n}=0$); for no-slip boundaries this condition is automatically satisfied if the magnetic field is made continuous at the surface.

2. DIMENSIONLESS EQUATIONS

In order to implement the dual time stepping and real time discretization as well as the MD for spatial integration it is better to write MHD equations in the following compact form:

$$\frac{\partial \mathbf{U}}{\partial \tau}+I_m\frac{\partial \mathbf{U}}{\partial t}+A\frac{\partial \mathbf{U}}{\partial x}+B\frac{\partial \mathbf{U}}{\partial y}=\mathbf{S}_v+\mathbf{S}^{\mathrm{ext}} \tag{24}$$

where

$$\mathbf{U}=[P',u,v,\theta,B_x,B_y,\Psi]^{\mathrm{T}} \tag{25}$$

is the state vector and $I_m=\mathrm{diag}[0,1,1,1,1,1,0]^{\mathrm{T}}$ is the diagonal matrix, which is used to eliminate the pressure and artificial magnetic relaxation function from the real-time advancements, and A and B are Jacobian matrices for x and y directions, respectively.

DOI: 10.1002/fld

3. TEMPORAL AND SPATIAL DISCRETIZATION

The real-time derivative in Equation (24) is approximated by the following second-order 3-level formula as done in [4]:

$$\frac{\partial \mathbf{U}}{\partial t} = \frac{3}{2\Delta t}(\mathbf{U}^{n+1} - \mathbf{U}^{n}) - \frac{1}{2\Delta t}(\mathbf{U}^{n} - \mathbf{U}^{n-1}) \tag{26}$$

and the pseudo time iterations were approximated by a third-order Runge–Kutta (RK) algorithm. When the pseudo iterations converge (i.e. $\partial \mathbf{U}/\partial \tau \to 0$), the time-accurate solution given by

$$I_m \frac{\partial \mathbf{U}}{\partial t} = \mathrm{Res}(\mathbf{U}, \beta^2, \delta^2) \tag{27}$$

is recovered from Equation (24) where

$$\mathrm{Res}(\mathbf{U}, \beta^2, \delta^2) = -A(\beta^2, \delta^2)\frac{\partial \mathbf{U}}{\partial x} - B(\beta^2, \delta^2)\frac{\partial \mathbf{U}}{\partial y} + \mathbf{S}_v + \mathbf{S}^{\mathrm{ext}} \tag{28}$$

is called the residual vector, which is discretized by an MD algorithm. By combining the real time levels with those of the pseudo time (written in explicit form for now), one gets

$$\frac{\mathbf{U}^{n+1,m+1} - \mathbf{U}^{n+1,m}}{\Delta \tau} + I_m \left[\frac{3(\mathbf{U}^{n+1,m+1} - \mathbf{U}^{n})}{2\Delta t} - \frac{(\mathbf{U}^{n} - \mathbf{U}^{n-1})}{2\Delta t} \right] = \mathrm{Res}^{n+1,m+1} \tag{29}$$

where $\mathbf{U}^n$ and $\mathbf{U}^{n-1}$ are frozen in pseudo iterations since there is no way of replacing them. By a slight modification of the above equation some implicitness can be introduced into the pseudo iterations obtaining a better algorithm than [4]

$$\frac{\mathbf{U}^{n+1,m+1} - \mathbf{U}^{n+1,m}}{\Delta \tau} = -I'_m \left[\frac{3(\mathbf{U}^{n+1,m} - \mathbf{U}^{n})}{2\Delta t} - \frac{(\mathbf{U}^{n} - \mathbf{U}^{n-1})}{2\Delta t} \right] + \mathrm{Res}^{n+1,m+1} \tag{30}$$

where $I'_m = [I + \frac{3}{2}(\Delta\tau/\Delta t) I_m]^{-1} I_m$ is the modified diagonal matrix and I is the unit matrix. In this way, the real-time derivative term was made explicit in pseudo iterations. Since the residual requires implicit treatment, the accuracy of the pseudo time derivative is improved by the following third-order RK algorithm so that the residual calculation for the next pseudo time iteration is more accurate (see [5]):

$$\begin{aligned}
\mathbf{U}^{(0)} &= \mathbf{U}^{n+1,m} \\
\mathbf{U}^{(1)} &= \mathbf{U}^{(0)} + 0.28\Delta\tau\,\mathrm{Res}^{*}(\mathbf{U}^{(0)}, \mathbf{U}^{n}, \mathbf{U}^{n-1}) \\
\mathbf{U}^{(2)} &= \mathbf{U}^{(0)} + 0.61\Delta\tau\,\mathrm{Res}^{*}(\mathbf{U}^{(1)}, \mathbf{U}^{n}, \mathbf{U}^{n-1}) \\
\mathbf{U}^{(3)} &= \mathbf{U}^{(0)} + \Delta\tau\,\mathrm{Res}^{*}(\mathbf{U}^{(2)}, \mathbf{U}^{n}, \mathbf{U}^{n-1}) \mathbf{U}^{(n+1),(m+1)} = \mathbf{U}^{(3)}
\end{aligned} \tag{31}$$

where

$$\mathrm{Res}^{*}(\mathbf{U}) = -I'_m \left[\frac{3(\mathbf{U}^{n+1} - \mathbf{U}^{n})}{2\Delta t} - \frac{(\mathbf{U}^{n} - \mathbf{U}^{n-1})}{2\Delta t} \right] + \mathrm{Res}(\mathbf{U}, \beta^2, \delta^2) \tag{32}$$

DOI: 10.1002/fld

As seen from Equation (31), the new pseudo values: $\mathbf{U}^{n+1,m+1}$ are obtained from $\mathbf{U}^{n+1,m}$ in three steps. As pseudo iterations converge (i.e. $\mathbf{U}^{n+1,m+1} \to \mathbf{U}^{n,m}$ so that $\mathrm{Res}^*(\mathbf{U}) \to 0$ and one gets the desired second-order accurate solution at new time level from $I_m \partial \mathbf{U}/\partial t = \mathrm{Res}(\mathbf{U})$ or

$$\mathbf{U}^{n+1} = \mathbf{U}^n + \tfrac{1}{3}(\mathbf{U}^n - \mathbf{U}^{n-1}) + \tfrac{2}{3}\Delta t\, I_m'^{-1}\mathrm{Res}(\mathbf{U}, \beta^2, \delta^2) \tag{33}$$

For the spatial discretization of the residual given in Equation (28), an MD scheme was utilized. In this scheme, it is assumed that the state vector, $\mathbf{U}$, changes linearly within the triangles (see [3] for details)

$$\mathbf{U}(x, y, t) = \sum_k \mathbf{U}_k(t) N_k(x, y) \tag{34}$$

where $\mathbf{U}_k(t)$ is the value of $\mathbf{U}$ at node k and $N_k(x_m, y_m) = \delta_{k,m}$ is the linear shape function. By multiplying Equation (24) by N_ℓ and integrating the result over domain Ω one gets (omitting pseudo time rate for now)

$$\iint_\Omega \left(N_\ell \frac{\partial \mathbf{U}}{\partial t} \right) \mathrm{d}\Omega = \iint_\Omega N_\ell \left(A \frac{\partial \mathbf{U}}{\partial x} + B \frac{\partial \mathbf{U}}{\partial y} \right) \mathrm{d}\Omega + \iint_\Omega N_\ell \mathbf{S}\, \mathrm{d}\Omega \tag{35}$$

By using Equation (34) the integral on the left-hand side of Equation (35) becomes

$$\sum_T \iint_\Omega \left(N_\ell \sum_{k=1}^{3} N_k \frac{\partial \mathbf{U}_k}{\partial t} \right) \mathrm{d}\Omega = \sum_T \iint_\Omega \sum_{k=1}^{3} N_\ell N_k \frac{\partial \mathbf{U}_k}{\partial t}\, \mathrm{d}\Omega$$

$$= \sum_{T \in \ell} \sum_{k=1}^{3} \frac{\Omega_T}{3} \delta_{\ell k} \frac{\partial \mathbf{U}_k}{\partial t} = \Omega_\ell \frac{\partial \mathbf{U}_\ell}{\partial t}$$

or including the pseudo time rate

$$= \Omega_\ell \left(I_m \frac{\partial \mathbf{U}_\ell}{\partial t} + \frac{\partial \mathbf{U}_\ell}{\partial \tau} \right) \tag{36}$$

where ℓ is one of the nodes of triangle T and Ω_ℓ is the median area around this node. By using the Gauss theorem, the flux integral in Equation (24) can be written as

$$\iint_\Omega \left(A \frac{\partial \mathbf{U}}{\partial x} + B \frac{\partial \mathbf{U}}{\partial y} \right) \mathrm{d}\Omega = \oint_{\delta\Omega} (\mathbf{F}\, \mathrm{d}n_x + \mathbf{G}\, \mathrm{d}n_y)$$

$$= \sum_{k=1}^{3} (A_k \mathbf{U}_k n_{k_x} + B_k \mathbf{U}_k n_{k_y}) \tag{37}$$

The same result can be obtained by first substituting Equation (34) into the flux integral

$$\sum_T \iint_\Omega N_\ell \left[A \sum_{k=1}^{3} \frac{\partial N_k}{\partial x} \mathbf{U}_k + B \sum_{k=1}^{3} \frac{\partial N_k}{\partial y} \mathbf{U}_k \right] \mathrm{d}\Omega \tag{38}$$

DOI: 10.1002/fld

and then using $\partial N_k/\partial x, y = n_{kx,y}/2\Omega_T$ since N is linear in T. Thus, Equation (38) turns into

$$\sum_T \iint_\Omega N_\ell \, \mathrm{d}\Omega \left[\sum_{k=1}^{3} A_k \frac{n_{k_x}}{2\Omega_T} \mathbf{U}_k + \sum_{k=1}^{3} B_k \frac{n_{k_y}}{2\Omega_T} \mathbf{U}_k \right]$$

$$= \left[\frac{1}{\Omega_T} \iint_\Omega N_\ell \, \mathrm{d}\Omega \right] \mathrm{Res}_T = B_\ell \, \mathrm{Res}_T \tag{39}$$

where

$$\mathrm{Res}_T = \sum_{k=1}^{3} \frac{1}{2} (A n_{k_x} + B n_{k_y}) \mathbf{U}_k = \sum_{k=1}^{3} K_k \mathbf{U}_k \tag{40}$$

where B_ℓ is the distribution matrix calculated at node k

$$K_k = \tfrac{1}{2} (A(\mathbf{U}_k) n_{k_x} + B(\mathbf{U}_k) n_{k_y}) \tag{41}$$

is the flux matrix whose eigensystem determines the spatial variation of flow quantities. Although one can use different distribution matrices (see [5]), the following Lax–Wendrof-type distribution matrix is used here:

$$B_\ell = \frac{1}{3} I + \frac{\Delta\tau}{2\Omega_\ell} K_\ell \tag{42}$$

where $\Delta\tau$ is found from the maximum eigenvalues of K_ℓ. The source in Equation (35) can be taken as the arithmetic average of nodal values:

$$\langle \mathbf{S} \rangle = \frac{\mathbf{S}_i + \mathbf{S}_j + \mathbf{S}_k}{3} \tag{43}$$

where i, j, k are the nodes of triangle T. By combining all the terms, the resulting algorithm turns into Equation (33) where the residual at node ℓ of triangle T is defined as

$$\mathrm{Res}_\ell(\mathbf{U}, \beta^2, \delta^2) = \frac{1}{\Omega_\ell} \left[B_\ell \sum_{k=1}^{3} K_k \mathbf{U}_k + \langle \mathbf{S} \rangle + \mathbf{S}_v \right] \tag{44}$$

where $\mathbf{S}_v$ is the viscous term, see [3] and references therein for details.

The solution procedure is that the residual given in Equation (44) is first calculated and distributed to the three nodes of triangles, which are visited once at each time step. The analytical boundary conditions are applied by just assigning analytical values at the boundary nodes. The outgoing or zero normal derivative boundary conditions are done by doing no action for these variables at the boundary nodes. The inherent structure of the MD scheme updates the variables to their correct values automatically.

4. NUMERICAL RESULTS

The numerical tests obtained from the code described so far will be presented in this section. Third-order RK algorithm, isotropic triangular mesh, $\beta^2 = 1$, $Pr = 0.72$ were used unless otherwise specified. The first few problems are classical benchmark tests and the last two tests are original tests including liquid metal flows.

DOI: 10.1002/fld

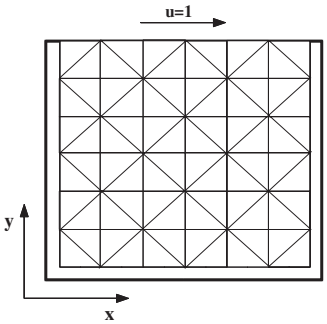

Figure 1. The solution domain for the steady-state lid-driven cavity test problem. The upper lid is moving to the right at constant velocity.

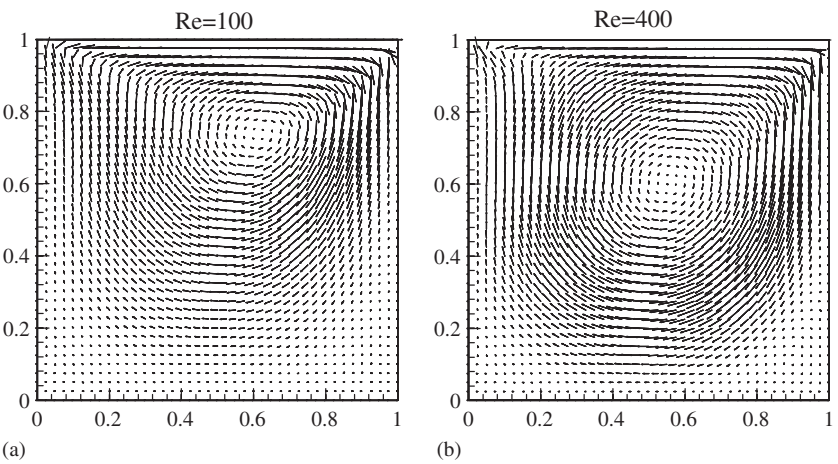

Figure 2. The velocity vectors in the cavity for: (a) $Re=100$ and for (b) $Re=400$.

4.1. Test 1: The steady-state (SS) lid-driven cavity test

The first test problem (taken from [6]) is the classical 2D SS lid-driven cavity test (a regular hydrodynamic flow with no heat transfer and electromagnetic fields). In this test, the sliding lid on the upper boundary with a constant horizontal velocity (i.e. $u=1$) drives a circulation in the cavity. As the stationary fluid impulsively starts to flow around the top lid, it creates a circulation and stagnation regions in the cavity depending on the viscosity of the fluid (i.e. inverse of Re number). The solution domain for this test was chosen as a square-shaped cavity filled with isotropic triangles with 41×41 nodes, see Figure 1 as a grid sample. Starting with no flow initial condition within the cavity, this test problem was run for $Re=100$ and for $Re=400$ with third-order RK algorithm using no-slip wall conditions (i.e. $u=v=0$) on the walls of the cavity and $u=1, v=0$ condition along its upper boundary. The resulting velocity vectors within the cavity, after steady state is achieved at $t=2$, are shown in Figure 2 for two different Re numbers. As can be seen, the constant flow along the upper lid drives the flow circulation whose centers shift as the Re number is increased

DOI: 10.1002/fld

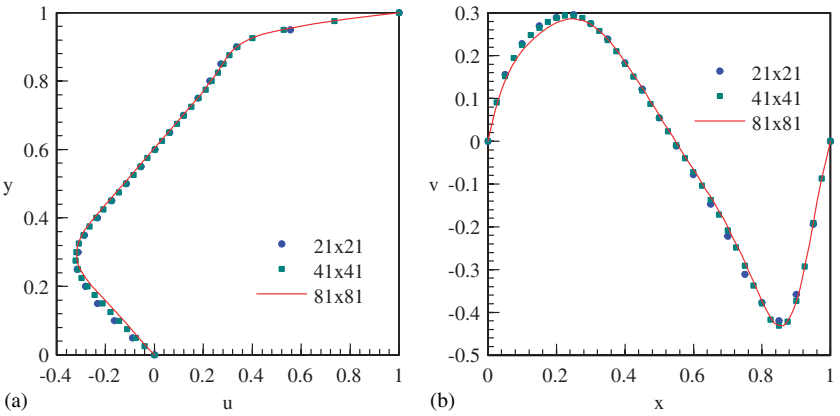

Figure 3. $y-u$ and $v-x$ profiles passing through the midpoint of the cavity.

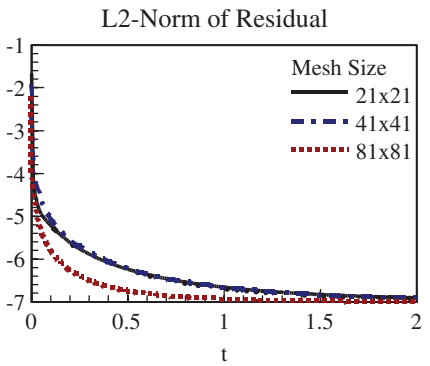

Figure 4. Time history of the L2 Norm of the residual calculated from all state variables.

from 100 to 400. Although invisible in the graphs, the lower corners of the lid include stagnant flow regions for $Re=400$ case. These results agree very well with those presented in Reference [6]. In order to check the convergence properties of the numerical scheme presented here, this test problem was run on three different isotropic meshes: 21×21, 41×41, and 81×81 and the SS values were obtained as before. The y profile of u velocity and x profile of v velocity passing from the midpoint of the cavity are presented in Figure 3. As can be seen, as the mesh gets finer the solutions convergence to the correct solution and the solution accuracy is rather reasonable even with the coarse mesh though no mesh refining is done near the walls. In order to have an idea about the convergence of the solutions, the L2 norm of residual (obtained from the maximum change of all flow variables) and the maximum velocity divergence are calculated for different meshes and the resulting time history of these quantities is shown in Figures 4 and 5, respectively. It is seen that the convergence is rapid and the error in velocity divergence reduces faster than that in the L2 norm. These solutions show that the code developed can be safely used for investigating the SS incompressible flows without the effects of electric and magnetic fields.

DOI: 10.1002/fld

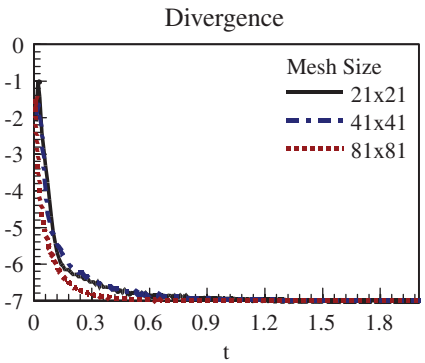

Figure 5. Time history of velocity divergence.

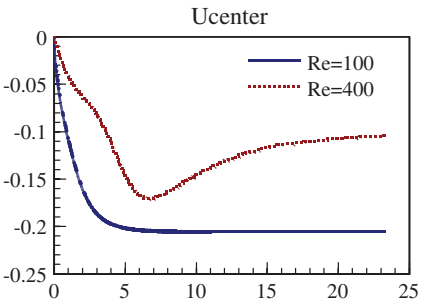

Figure 6. Time history of the u velocity at the midpoint of the cavity for $Re=100$ and $Re=400$.

4.2. Test 2: The unsteady lid-driven cavity test

In this test, the same square cavity, the same initial and the same boundary conditions were chosen and the time behavior of u velocity at the midpoint of cavity is investigated. Initially zero flow was chosen in the cavity and the lid's velocity was given by a step function, which is defined by $u=0$, $t<0$, and $u=1$, $t>0$. This impulsively starting flow test was solved for two different Reynolds numbers: $Re=100$ and $Re=400$ in order to examine transient behavior of the solutions. With the time step of $\Delta t=0.01$, the problem was solved by third-order RK algorithm on an 81×81 isotropic structured mesh. The time histories of u velocity at the midpoint of the cavity for two different Re numbers are shown in Figure 6. As seen, the velocity at the center reaches two different SS values for different Re numbers. These results are in excellent agreement with the results of Dailey and Pletcher [6]. This result shows the rather satisfactory temporal accuracy of the numerical scheme.

4.3. Test 3: Unsteady oscillatory lid-driven cavity test

This test is similar to the previous tests except that in this case the velocity for the upper lid was assumed to be time periodic as $u(t)=u_0\cos t$. In that case, since the flow inside the cavity is controlled by sinusoidally changing lid velocity, the solutions are expected to reach a periodic stage after a certain amount of time. To follow how these periodic oscillations are reached, the

DOI: 10.1002/fld

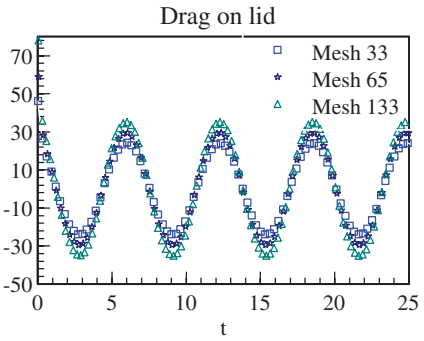

Figure 7. Drag on the upper lid as a function of time.

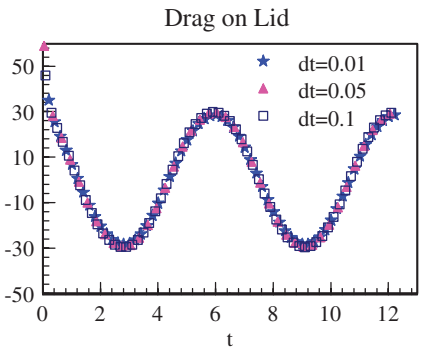

Figure 8. Drag on the upper lid for three different time steps on a 65×65 mesh.

temporal behavior of the drag on the upper lid was examined. The drag on the upper lid was calculated from

$$D = \int_{x=0}^{1} \left(\frac{\partial u}{dy} \right) \Bigg|_{y=1} \mathrm{d}x$$

by using a simple trapezoidal integration method.

Reynolds number was taken as 400 and this problem was run on three different isotropic meshes, i.e. 33×33, 65×65, and 133×133, and the time behavior of the drag on the upper lid is depicted in Figure 7. As can be seen, the drag reaching a maximum of 30 becomes periodic in a short period of time agreeing very well with the result presented in [7]. The same problem was then run on a 65×65 mesh by using three different time steps ($\Delta t = 0.01, \Delta t = 0.05, \Delta t = 0.1$) and the resulting graphs were depicted in Figure 8. It is obvious from these results that the effect of the time-step selection is negligible in obtaining time-accurate solutions. These results show that the numerical scheme presented here has a very good temporal accuracy being independent of the time-step selection. It must be noted here that when a large time step is used, the number of pseudo iterations slightly increases in order to achieve the pre-specified numerical accuracy.

DOI: 10.1002/fld

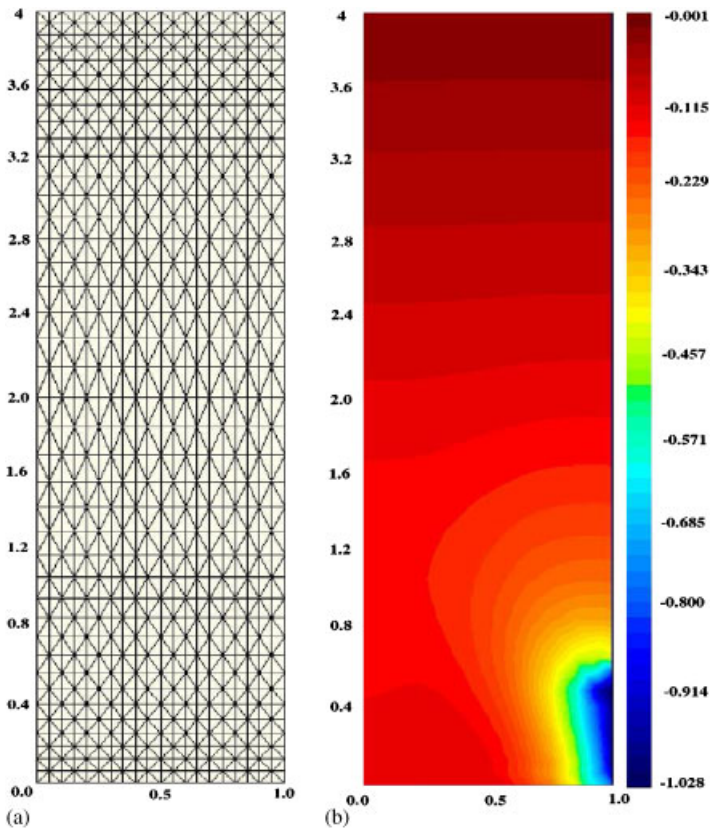

Figure 9. (a) The structured isotropic 21×41 mesh, which gets finer at the top and bottom of the channel and (b) the pressure contours in the vertical channel.

4.4. Test 4: Vertical obstructed flow through square channels

The channel flows, which are driven by the pressure difference between inlet and outlet are of great importance in pipe flows, suction machines, internal flow cavities, etc. In this test, a rectangular channel of aspect ratio 4 is considered to examine the vertical flow exiting on the side wall in the presence of a rectangular wall obstruction or rib. In this case, the isotropic mesh used includes 21×41 points (with a mesh size of $x:(0\text{–}1)$, $y:(0\text{–}4)$) but it is made finer near the top and the bottom of the channel as shown in Figure 9(a). It is assumed that $Re = 100$, $\beta^2 = 10$, $Pr = 0.72$ and that the side walls are no-slip walls but the right wall has an outlet opening of width 1.0 starting from the bottom. The pressures at the upper and lower boundaries were set to 0 and -1, respectively in order to drive flow in $-y$ direction and the outgoing velocity conditions are used on the inlet and outlet, so that velocity profiles at these boundaries are automatically determined by the scheme. A typical pressure colour graph after SS is established for the no-obstruction case is shown in Figure 9(b). When there is no obstruction in the channel, the vertical parabolic velocity profile bends towards the opening on the side wall and a small circulation region is created on the lower left corner as clearly seen from Figure 10(b). When rectangular obstruction is placed on the

DOI: 10.1002/fld

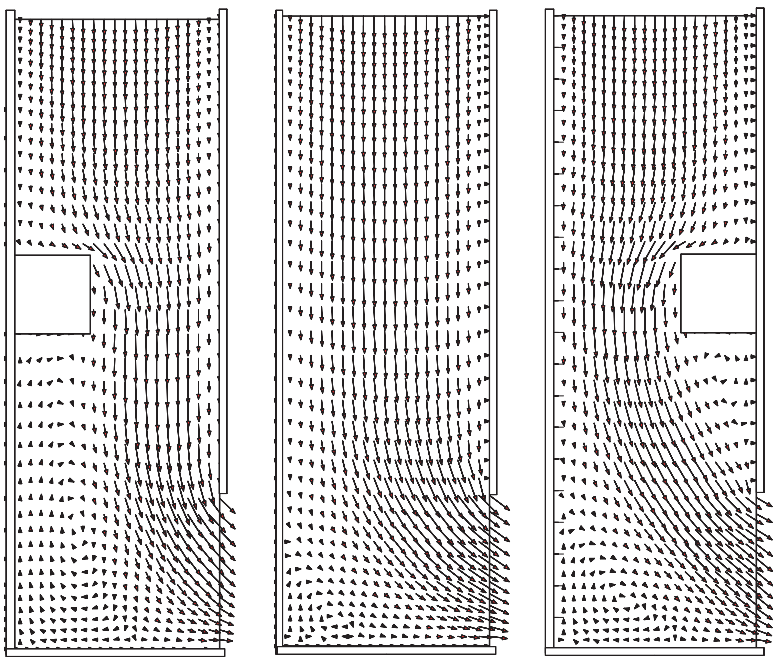

Figure 10. The vertical channel natural flow in the presence of square obstruction along the side walls.

right wall, not only does this corner circulation region get bigger but also a new circulation region emerges below the square obstruct. When the square obstruct is on the left wall, the circulation regions in the corner and below the obstruct converge creating a wider circulation region. These results are of great importance since the pipe design is done by first examining possible flow behavior under specified conditions.

4.5. Test 5: Natural flow in thermally driven cavity by different side wall temperatures

Natural convection heat transfer inside cavities is important in a wide range of applications such as room insulation, ventilation and cooling of electronic components, solar cavity receivers, etc. This is the classical benchmark problem of Davis [8] in which $Pr=0.71$ was taken and BA is used. Owing to this temperature gradient because of constant temperature walls (hot on the left cold on the right), naturally circulating flow develops due to the Buoyancy effects of gravity. In order to have the same normalization and the same dimensionless viscosity, $Re=1.408=1/Pr$ was chosen and two cases with $Ra=10^4$ and $Ra=10^5$ were considered along with a large artificial compressibility parameter of $\beta^2=100$. Note that a higher Rayleigh number requires greater β^2 in order for viscous and flux terms to have the same order of magnitudes. This test was solved on a 61×61 isotropic mesh to obtain the steady-state solutions. The temperature contours for two different *Ra* numbers are shown in Figure 11. As can be seen from these graphs the thermal boundary layer along the side walls gets thinner as *Ra* number is increased. These results agree

DOI: 10.1002/fld

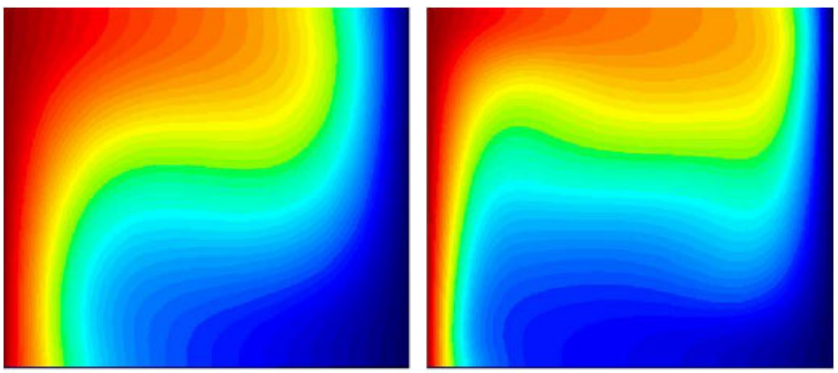

Figure 11. Temperature profile for $Ra = 10000$ and $Ra = 100000$ for thermally driven cavity.

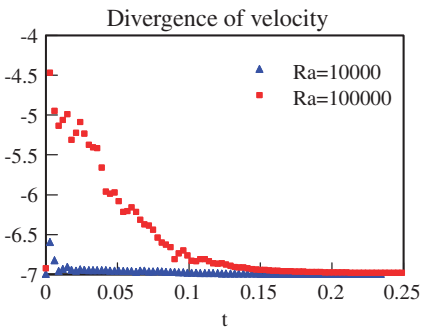

Figure 12. Maximum logarithm of the velocity divergence magnitude in the mesh.

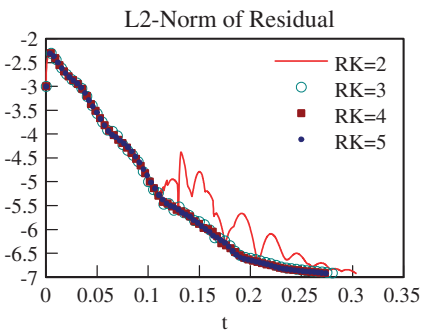

Figure 13. L2 norm of residual for thermally driven cavity test.

DOI: 10.1002/fld

very well with those in [8] since the maximum values of u and v vary between 16.064–16.182 and 19.514–19.614 for $Ra=10^4$ and 33.965–35.070 and 67.562–68.844 for $Ra=10^5$ as given in Table I of [9]. The results presented here agree very well with those results since maximum velocities are 16.136 and 19.605 for $Ra=10^4$ and 35.355 and 69.055 for $Ra=10^4$. In order to examine the temporal evolution of velocity divergence, the maximum logarithm of velocity divergence in the mesh is shown in Figure 12 for $Ra=10^5$ and $Ra=10^4$. The convergence of pseudo iterations gets poorer as Ra number is increased. This is due to the fact that a finer mesh is needed when the thermal boundary layer is thinner. This behavior also explains why the numerical errors in maximum velocity increase as Ra number increases. To see the difference in the residual drop due to different RK orders, the problem was solved for second- to fifth-order RK algorithms and the results are depicted in Figure 13. The solutions are assumed to have reached SS as the L2 norm of the maximum mesh residual drops to -7.0, which almost corresponds to machine zero. It is clear that the solution has minor fluctuations for second-order RK level, while the other levels produce almost identical behavior. This is the reason why, in this research, usually the third-order RK steps are used for best accuracy and fewer pseudo iterations.

Having shown that the code presented here works accurately for a totally hydrodynamics case, two more test problems will be presented next in order to demonstrate the effectiveness of our algorithm in solving MHD equations.

4.6. Test 6: Liquid metal flow past a circular cylinder in open channels exposed to external magnetic field

This problem describes conducting incompressible liquid metal flow past a circular cylinder when the medium includes a vertical or parallel magnetic field. The flow around the cylinder becomes unstable and vortices start to shed from the cylinder surface behind which periodic flow is obtained for both $Re=100$ and $Re=400$. It is shown in this test that such flows can be stabilized by using an external magnetic field. The cylinder with a radius of unity was placed at $(x=0, y=0)$ in a computational domain of $(-4.5\leqslant x\leqslant 15.5, -4.5\leqslant y\leqslant 4.5)$. The inflow boundary condition was used on the inlet (left surface) with $u=1, v=0, B_{x,y}=1$ and reflecting boundary conditions were used on upper and lower boundaries with $v=0, B_{x,y}=1$. The right boundary was chosen as the outgoing boundary on which no condition was imposed on velocity but $B_{x,y}=1$ was taken when magnetic fields exist. The cylinder surface is taken as no-slip boundary with $u=v=0$ and $B_{x,y}=1$. This problem was run for no magnetic field, with a parallel field (in x direction) and with that in y direction for $Re=100$ and $Re=400$. The interaction parameters were chosen as $0, 0.001, 0.0625, 0.25$ corresponding to Hartmann numbers of $0, 1, 2.5, 5.0$, respectively, for magnetic Reynolds number of 10^{-5}. These parameters were chosen to compare the results with those presented by Armero and Simo [10] who solved the problem with only horizontal magnetic field (i.e. $B_x\neq 0$ and with only $Re=100$); however, the effects of vertical field are also examined in this work. Figure 14 shows the time behavior of x-velocity contours at times $t=0, 30, 60, 90, 120, 150$ for $Re=100$ and $Re=400$ with no magnetic field . The final figure in the left and the top left graph of Figure 12 of [10] has excellent agreements. When $B_x=0$ and $B_y=1$ is used as a boundary condition, this field eliminates the transient oscillations and finally the periodic behavior when Hartmann number is high enough and Re number is not greater than 100. The temporal behavior of the solutions at $Re=100$ and $Re=400$ for $N=0.25$ $(Ha=5)$ is given in Figure 15. As can be seen, the vertical magnetic field eliminates oscillations for $Re=100$ but does not work efficiently for $Re=400$. The final figure on the left corresponds to the second graph from the bottom of Figure 12 of [10] with

DOI: 10.1002/fld

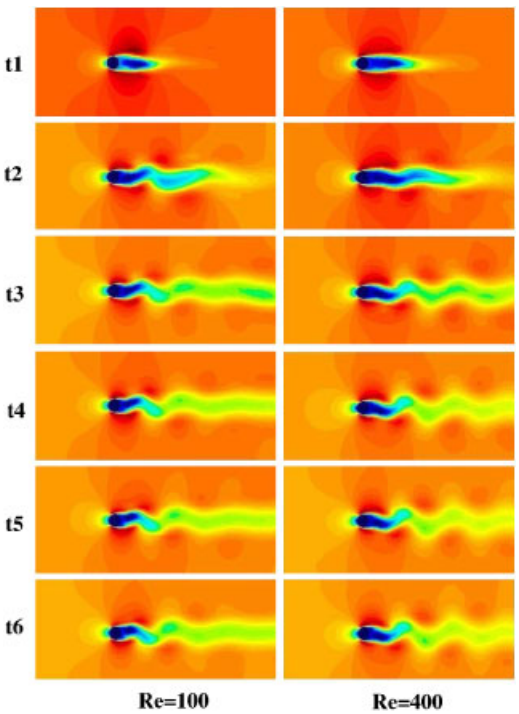

Figure 14. The contour graphs and time behavior of u-velocity at $Re=100$ (left) and $Re=400$ (right) when no fields exist, i.e. $N=0$ ($Ha=0$).

an excellent agreement again. The same problem was then run for $Re=100$ in the existence of horizontal magnetic field ($B_y=0, B_x\neq 0$) at different strengths (i.e. different Hartmann numbers) and the results are given in Figure 16. While examining these figures one can infer that the horizontal magnetic field does a better job of eliminating oscillations at $Re=400$ even at lower Hartmann numbers. The addition of a magnetic field in a conducting medium adds viscosity and creates an extra drag on the immersed body. These effects are of great importance for metal casting in atmospheric pressures and thin film deposition in vacuum chambers.

4.7. Test 7: Electromagnetic braking of liquid metals in vertical channels and levitation

The flow control of liquid metals is important for both the MHD generator and the heat transfer problems. In MHD generators, the heated liquid metal arrives in the downcomer passing through a narrow channel with two faces of metallic back and front electrodes and magnetized and isolated electrodes on its sides. In his collaboration with Danieli Steel Corp. Italy, Tessarotto proposed a DC scheme of applying external electric and perpendicular magnetic field in order to slow down or levitate liquid metals by his $(1+\frac{1}{2})$-dimensional calculations, see [11]. As was shown in this reference, the levitation of liquid metal flowing down through a rectangular channel was possible provided that external field strengths were appropriate. In his calculations, the averaged vertical velocity, which reached its steady value of $-1.5\,\mathrm{m/s}$, when the electric and magnetic fields were

DOI: 10.1002/fld

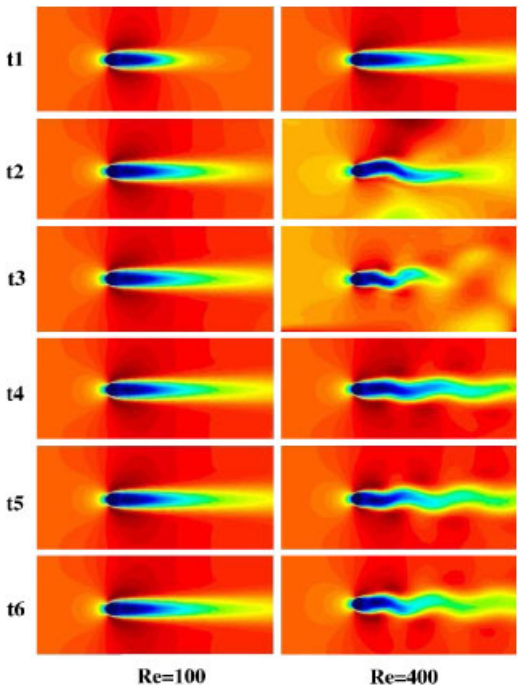

Figure 15. The contour graphs and time behavior of u-velocity at $Re=100$ (left) and $Re=400$ (right) when a perpendicular field (B_y) exists for $N=0.25$ ($Ha=5$).

switched on and then the magnitude of perpendicular velocity dropped to zero exhibiting a series of damped oscillations. The same numerical experiment was done here with the two-dimensional code presented here. As an illustration of the experiment performed in Reference [11], the three-dimensional structure of the liquid metal flow control region is shown in Figure 17(b). As can be seen from this figure, external magnetic field is applied perpendicular to the flow direction (i.e. x direction) through coils and the external electric field is applied in z direction (perpendicular to solution domain). In that case, the direction of $\vec{\mathbf{E}}\times\vec{\mathbf{B}}$ force opposes the gravitational force, which is in $-y$ direction. The applied electric and magnetic field vectors and the coil-winding directions are depicted in Figure 17(c) as top view. The fields are applied on the rectangular plane (i.e. the solution domain) as shown in Figures 17(a,b). The external magnetic field is given as the following analytical value by solving $\nabla^2 A_z=0$ where A_z is the vector potential satisfying $\vec{\mathbf{B}}^{\text{ext}}=\nabla\times\vec{\mathbf{A}}$ where $\vec{\mathbf{B}}^{\text{ext}}$ satisfies $\nabla\times\vec{\mathbf{B}}^{\text{ext}}=\mathbf{0}$ and $\vec{\nabla}\cdot\vec{\mathbf{B}}^{\text{ext}}=0$. The solution of the vector potential is $A_z=\cos h(\lambda x)\sin(\lambda y)$ where λ is a free parameter whose value should be adjusted according to suitable boundary conditions. In that case, the external field becomes

$$B_x^{\text{ext}}=B_0\cos h(\lambda x)\cos(\lambda y),\quad B_y^{\text{ext}}=-B_0\sin h(\lambda x)\sin(\lambda y) \tag{45}$$

where $B_0=1$ was taken. Figure 18 gives the temperature contours, standard vertical parabolic velocity vectors and the vector graph of total magnetic field within the solution domain (with $\lambda=1.0$) just after the switch was turned on at $t=2$. Note that at that instant the internal magnetic

DOI: 10.1002/fld

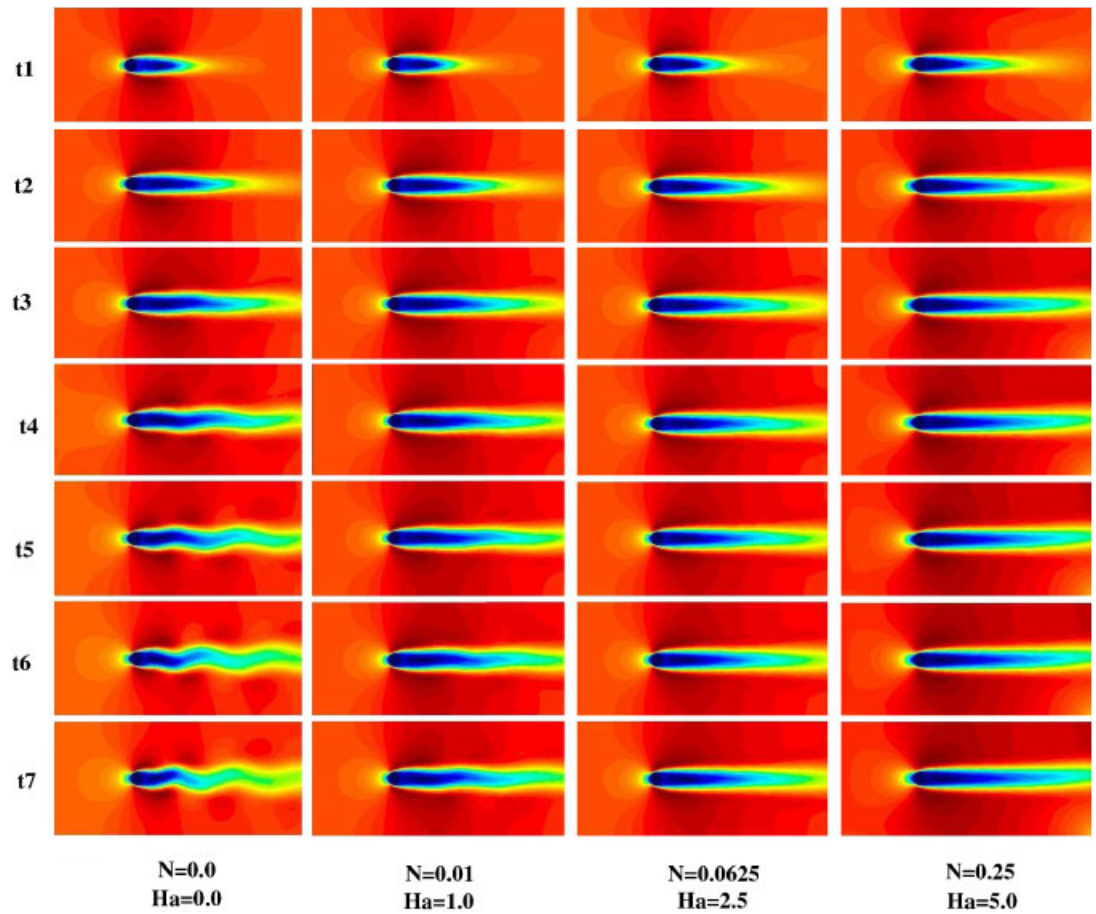

Figure 16. The time behavior of the flow around the cylinder at different interaction parameters for $Re=100$ and $B_y=0$, $B_x\neq 0$.

field is negligible in comparison with the external one; hence, Figure 18(c) can be considered to be the graph of only $\vec{\mathbf{B}}^{\text{ext}}$.

In this test, the external fields are turned on by a switch when the vertical flow of $v=-1.5$ was given as initial condition with $Re=1000$, $Ra=100$, $Re_{\text{m}}=5$ and $Pr=0.72$, $\Delta t=0.005$. Note that the steady vertical flow under gravity can be provided as the initial condition or it can be obtained by running the code without fields and then switching on the fields after a prescribed time. In that case, the vertical flow is modified and begins to display small oscillations whose intensity and period depend on the interaction parameter, N and the strength of external electric field, i.e. E_0, and that of the external magnetic field, B_0. As the boundary conditions, no-slip $(u, v=0)$ and constant temperature $(T=0.5)$ boundary conditions were applied along the walls at $x=\pm 0.5$, which are assumed to non-ferromagnetic and non-conducting (i.e. $\partial\vec{\mathbf{B}}/\partial x=0$). The top (inlet) boundary was considered to be at constant temperature $(T=1)$ and pressure $(P=0)$ and the bottom boundary was taken as outgoing boundary at which pressure was defined to be $P=-1$

DOI: 10.1002/fld

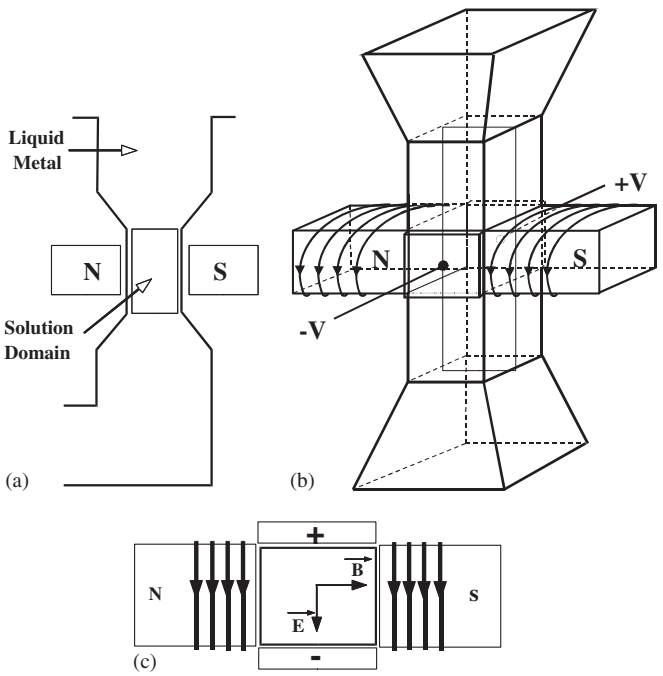

Figure 17. The whole industrial system for electromagnetic braking applications.

and the other fields were kept untouched. In this case, the pressure difference and gravity cause the increase in vertical downward flow and external fields slow it down in a short span of time after the switch is turned on. A DC electric field perpendicular to solution domain is applied by connecting the electrodes (in contact with the liquid metal) to a DC power supply. The magnetic field was also applied simultaneously by turning on coil currents. Since the electric field is perpendicular to the solution domain, one needs no boundary condition for electric field. Note that the hydrodynamic flow state can be obtained in two different ways before the application of external fields. In the first, a homogeneous vertical velocity ($u=0, v=-1.5$) can be given everywhere in the mesh as the initial condition. In that case, the code converges quickly to the homogeneous parabolic velocity profile as shown in Figure 18(b). In the second, zero velocity and constant pressures on the top and bottom boundaries ($P_{\text{top}}=0, P_{\text{bottom}}=-1$) can be given as the boundary condition. In that case, hydrodynamic convergence takes time (as shown in Figure 19). The time dependence of the vertical velocity at the center of exit after its steady value ($V_y=-1.5$) is changed when the switch is turned on, as shown in Figure 19. When the external fields are applied, the vertical flow slows down and stops after a short time period after passing through minor oscillations. This behavior is obvious from Figure 19 with two different values of interaction parameters, $N=2$ and $N=0.5$; obviously, $N=0.5$ giving a better control with less oscillations. After running this problem with different N values it was found that the optimum value was found to be $N=0.4$. The time rate of central vertical velocity at the outlet with $N=0.4$ and its long time behavior are presented in Figure 20. As can be seen, as far as the external fields are kept on, the flow remains stopped at the outlet of the channel for a very long time.

DOI: 10.1002/fld

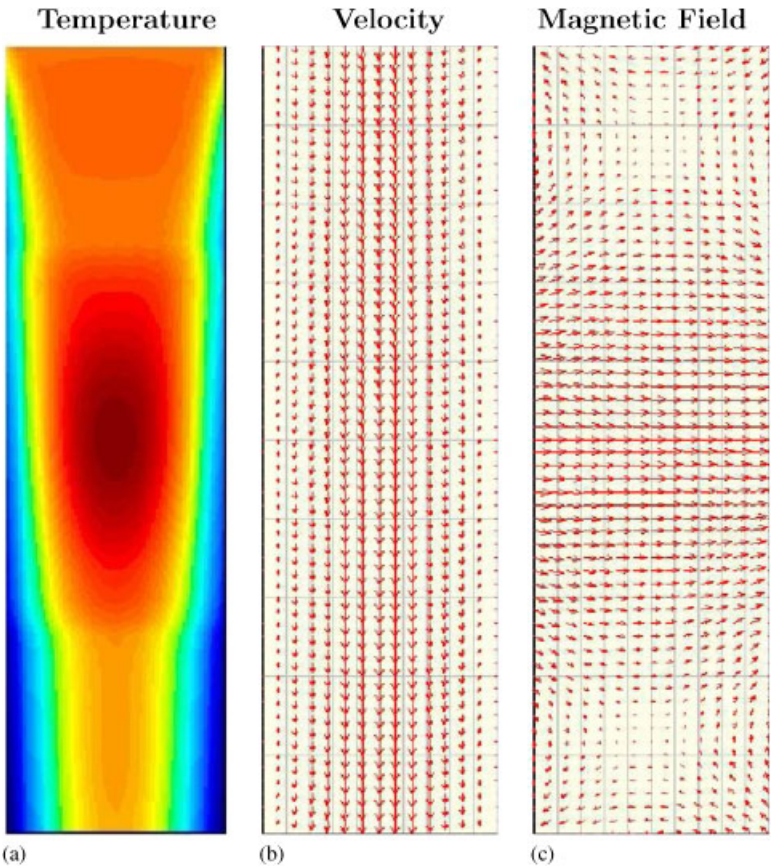

Figure 18. Temperature profile, velocity and magnetic field vectors in the channel just after external fields are turned on.

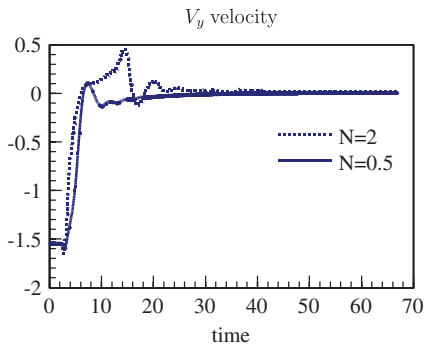

Figure 19. The effect of the interaction parameter, N, on the vertical velocity when external electric and magnetic fields are turned on at $t=2$ simultaneously.

DOI: 10.1002/fld

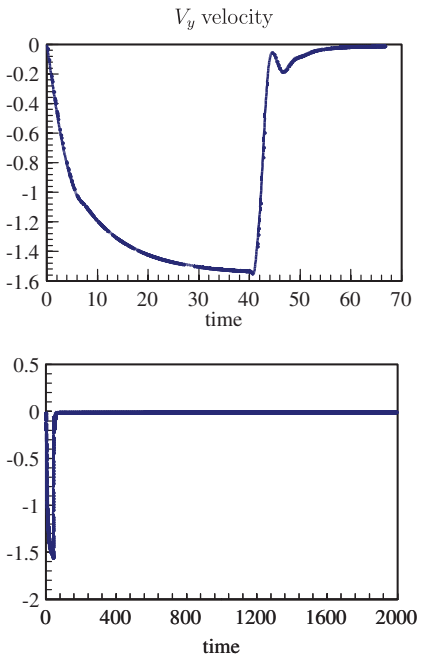

Figure 20. Vertical velocity profile and its long-time behavior with $N = 0.4$ when the external fields are applied (at $t = 40$) after steady state is reached.

5. CONCLUSION

A numerical scheme is presented to solve incompressible MHD equations for channel flows including BA, effects of heat transfer, and the existence of external and internal electric and magnetic fields for liquid metal flows. A Lax–Wendrof-type MD algorithm is used along with a dual time-stepping scheme and third-order RK steps. The code includes an artificial magnetic relaxation function and utilizes the artificial compressibility method in order to handle numerical difficulties in satisfying the divergence conditions on the velocity and magnetic fields. It is shown by numerical results that the code is accurate and robust and that it can be safely run for a variety of 2D varying from simple natural flow to heated liquid metal flows under the effects of external and internal sources.

ACKNOWLEDGEMENTS

The partial supports from the University of Trieste and the ICTP, Italy are appreciated. The financial support by Tubitak, Turkey through the COST project:TBAG-U/166 (105T547) is also acknowledged.

REFERENCES

1. Chorin A. A numerical method for solving incompressible viscous flow problems. *Journal of Computational Physics* 1967; **2**(1):12–26.

DOI: 10.1002/fld

2. Dedner A, Kemm F, Kroner D *et al*. Hyperbolic divergence cleaning for the MHD equations. *Journal of Computational Physics* 2002; **175**:645–673.
3. Aslan N, Onbasioglu E, Erdogan A. Parallelization of visual magneto-hydrodynamics code based on fluctuation distribution scheme on triangular grids. *Computers and Fluids* 2007; **36**:961–973.
4. Rogers SE, Kwak D. Upwind differencing scheme for the time-accurate incompressible Navier–Stokes equations. *AIAA Journal* 1990; **8**(2):253–262.
5. van der Weide E. Compressible flow simulation on unstructured grids using multi-dimensional upwind schemes. *Ph.D. Thesis*, von Karman Inst., Sint-Genesius-Rode, Technische Universiteit Delft, 1998. ISBN: 90-5623-067-0.
6. Dailey LD, Pletcher RH. Evaluation of multigrid acceleration for preconditioned time-accurate Navier–Stokes algorithms. *Computers and Fluids* 1996; **25**(8):791–811.
7. Granier B, Lerat A, Wu Z-N. An implicit centered scheme for steady and unsteady incompressible two-phase flows. *Computers and Fluids* 1997; **26**(4):373–393.
8. de Vahl Davis G. Natural convection of air in a square cavity: a bench mark numerical solution. *International Journal for Numerical Methods in Fluids* 1983; **3**:249–264.
9. Rubido O, Bravo E, Claeyssen JR. Thermally driven cavity flow with Neumann condition for the pressure. *Applied Numerical Mathematics* 2002; **40**:327–336.
10. Armero F, Simo JC. Long-term dissipativity of time stepping algorithms for an abstract evolution equation with applications to the incompressible MHD and Navier–Stokes equations. *Computer Methods in Applied Mechanics and Engineering* 1996; **131**:41–90.
11. Codutti A, Martinis A, Pavlicevic M, Tessarotto M, Batic D. Mathematical modelling and experimental model validation for a DC electromagnetic valve for liquid steel. *Proceedings of EPM2000 3rd International Symposium on Electromagnetic Processing of Materials*, Nagoya, Japan, published by The Iron and Steel Institute of Japan, 2000; 530.

DOI: 10.1002/fld